Carbon Trends 8 (2022) 100174

Contents lists available at ScienceDirect

Carbon Trends

journal homepage: www.elsevier.com/locate/cartre

Distinguishing of carbons and oxidation behaviour (Part 1): Exploring model-free kinetics and RAMAN spectroscopy as a synergistic approach for evaluating carbon-bonded-refractories

Ebrima Sallah[a,*], Wafaa Al-Shatty[b,c,*], Cameron Pleydell-Pearce[a,*], Andy J. London[d], Chris Smith[d]

[a] Materials Research Centre, Swansea University, Bay Campus, Swansea SA1 8EN, GB, United Kingdom
[b] Energy Safety Research Institute (ESRI), Swansea University, Bay Campus, Swansea SA1 8EN, United Kingdom
[c] Laboratory and Quality Control Department, Basrah Oil Company, Bab Al Zubair, Basrah 21240, Iraq
[d] Material Research Facility, UK Atomic Energy Authority, Culham Science Centre, Abingdon, OX14 3DB Oxfordshire, GB, United Kingdom

ARTICLE INFO

Article history:
Received 30 January 2022
Revised 11 April 2022
Accepted 12 April 2022

Keywords:
Model free kinetics
Carbon bonded refractory
Submerged Entry Nozzle
Raman Spectroscopy
Oxidation

ABSTRACT

A rapid synergetic profiling approach to determining oxidation behaviour and distinguishing of carbons within a refractory composite was explored for steel end user application. The efficacy for both Raman spectroscopy and model free kinetics were studied and proved successful for adoption as routine techniques. With the model free approach, the complex reaction steps were profiled as a multi-step reaction with series of activation energy ranging from 230 KJ/Mol to 150 KJ/Mol. The complex oxidation behaviour was supported by high temperature Raman spectroscopy which corroborated the pore closure mechanism that plays a critical role in modulating reaction intensity. Raman tracked oxidation via its effect on the crystallite sizes of resin (~ 5.5 nm to 8.5 nm) and intensity peak ratio of D to G peak within some limitations that are discussed in the study. Lastly, an empirical prediction of isothermal experiment from non-isothermal kinetics was validated and considered useful for determining the life of carbon especially in cases where under performance was suspected due to improper preheating by the end-user.

1. Introduction

Carbons present in carbon bonded refractories are known to help against corrosion, physical impact of molten steel, and resistance to thermal shock effects [1–4]. The degradation of carbons therefore implies deterioration of the same properties. These products are heavily relied upon within the steel industry, as they form parts of vessels and furnaces that contain the molten metal [3–6].

The composite investigated in this study comes from a refractory product called a submerged entry nozzle (SEN) [2,7]. The SEN creates the passageway needed to control the flow of molten steel during the continuous casting process or solidification process of molten steel [2,3,7]. It is comprised of a carbonaceous matrix, in the form of a phenolic resin binder system and graphite flakes [3,8,9]. It also has a predominant aggregate system made up of high melting point oxides [2,3,7,9].

Improper heating of the SEN during its preparation for contact with molten steel can result in unwanted oxidation and thermo-mechanical compromise, leading to failures with unexpected costly delays in production, for steel producers [10–12]. Finding a suitable, rapid, and robust profiling tool for assessing the mineralogical resistance to oxidation can alleviate concerns for steel users on the performance aspect of the SEN. It also gives them a tool to assess when in fact mineralogical changes have an impact whether it be from their own process of heating the product or how it was made i.e., as a quality assurance measure. This is key to distinguishing the origins of failure and product benchmarking.

The carbonaceous matrix, although extremely useful for the SEN as mentioned previously, is highly susceptible to oxidation at temperatures greater than 400 °C [3,13]. The thermal oxidation stability of the carbons inherently depends on their raw material quality, size, quantity, distribution, and their processing history to form part of the bulk refractory product [3,13]. The kinetics of oxidation are sensitive to both carbon reactivity (chemical kinetics) and the pore structure within the bulk (in the case of diffusion kinetics) [3,13]. Pore sensitivity is more pronounced at higher temperatures where diffusion kinetics starts to dominate

* Corresponding authors.
E-mail addresses: sallahebrima@ymail.com (E. Sallah), c.pleydell-pearce@swansea.ac.uk (C. Pleydell-Pearce), andy.london@ukaea.uk (A.J. London).

https://doi.org/10.1016/j.cartre.2022.100174

over chemical reactivity/kinetics. Pore structure and chemical reactivity are both influenced by the mineralogical grade and the way in which the product is manufactured and treated thereafter [3,13]. Both factors have a critical role in kinetics [3,13]. This study assesses the feasibility of using model free kinetics methods (static and conversion-based model) and Raman spectroscopy for distinguishing and profiling oxidation behaviour in a carbon bonded refractory SEN [14,15]. To the best knowledge of authors, the kinetic profiling employed here and its synergy with Raman spectroscopy is rarely applied to carbon bonded refractories.

In terms of model free kinetics, similar approaches have been employed for phenolic composites but focused mainly on topic related to synthesis, curing kinetics and pyrolytic kinetics [16–19]. There is a lack of data pertaining to values of oxidation activation energy and mechanism of degradation of the resin phase within a bulk carbon bonded refractory composite, post synthesis. The closest study found was conducted by Wang et al. 2006., who analysed the kinetic oxidation behaviour of a normal phenolic resin against a modified phenolic composite resin (by addition of silicon and lignin-derivative phenol), utilising model free kinetic. Their study focused solely on the non-conversion method and synthesis of resin [20].

Others have analysed the kinetics of resin derived non-graphitizing carbons using different approaches in applications other than refractories and have reported activation energy values ranging from 120 – 260 KJ/mole [21–23].

The synergistic approach of utilising Raman spectroscopy and model free kinetics opens opportunities for rapid fingerprinting, behavioural evaluation and distinguishing of carbonaceous phases. These are all useful parameters for metallurgical end-users. Raman is exceptionally powerful in elucidating the chemical structure of graphitic and polyaromatic compounds found within the refractory of concern [8,24]. It permits identification of chemistry, calculation of nano-crystallite size, defect detection and its quantification [8,24].

Model free kinetics has the potential to shed new insight regarding oxidation behavioural complexities of refractories by tracking changes in activation energy during oxidation and determining the unique mechanistic profile without the need of solid-state kinetic model force-fitting model with predefined sample geometries [14,15]. Model free requires very minimal number of samples to run (3 variable heating rates) [25]. It takes less time to conduct and allows small variability within sampling for ease of use (weight within ± 5% in specific cases) [14,15,26]. It can also be used for predicting isothermal experiments [27]. All of which make it an effective alternative for end-users. The following points are investigated in this study:

- The ability to track oxidation behaviour with Raman spectroscopy
- The meanings behind the practical application of the non-conversion model of Kissinger and Ozawa.
- The conversion-based method is applied in order to gain a better insight into the complexities of oxidation reaction behaviour supported by high temperature Raman analysis.

This study aims to verify whether these techniques can meet the needs of metallurgical users by offering an alternative rapid test methods when trialling out new products, indicating on performance and benchmarking against their process.

2. Experimental

2.1. Materials

SEN samples were provided by steel TATA-Steel Strip UK ltd. Attenuated total reflection (ATR)-FTIR spectroscopy by Themo Scientific (Nicolet iS10) was used to identify the main composite constituents of the SEN. The scan range was from 500 – 4000 cm^{-1}.

According to the FTIR data, the constituents of the aggregates were mainly alumina and silica, based on peaks identified in the range 951 cm^{-1} to 1381 cm^{-1} [28–30]. The peak at 951 cm^{-1} is also attributable to C–H bending vibration of sp2 hybridized bonding [31]. 1973.4 cm^{-1}, 2031.7 cm^{-1} and 2152.2 cm^{-1} are diamond peaks of the instrument [32,33]. The peak at 3645 cm^{-1} is attributable to adsorb water and O–H stretching [30,34]. 2980.5 cm^{-1} and 2881.7 cm^{-1} are Al–O and alkane C–H stretching, respectively [34,35] (Supporting information: Figure S1).

2.2. Characterisation techniques

2.2.1. Themo-analytic analysis/calorimetry

TA thermal analysis instrument, SDT Q600 was used to simultaneously measure weight change and heat flow characteristics of bulk carbonaceous composite.

- For both non-conversion and isoconversion method, heating rates of 3, 11, 27 °C/min were employed. Purged gas using air at 100 ml/min was applied on samples. Sample weight for oxidation test was approximately 17±3 mg. TA software was used for obtaining data derivatives and conversion which were then exported to excel for further data treatment.
- For experimental validation and evaluation of the predicted reaction rates, three isothermal oxidation experiments were conducted at 510 °C, 540 °C and 570 °C. Initial gas purge was with argon at 95 ml/min until the required temperature was reached before switching to air at 100 ml/min.
- For the Raman study, 4 separate samples were oxidised at isothermal temperature of 510 °C, with time stamps of 1,2,3, and 4 min. The same gas purge treatment as above was used, switching between argon and air.

Samples were all placed on an alumina pan of 90 μl, with a balance sensitivity of 0.1 μg and inserted into the bifilar wound furnace of the SDT Q600. Platinum-Rhodium (Type R) thermocouples are used to monitor the temperature which is equipped with a DTA (differential thermal analysis) sensitivity of 0.001 °C.

2.2.2. Raman spectroscopy

WiTec Alpha 300R Raman laser microscope was used to conduct depth scans. Oxidised samples were analysed with scan width of 80 µm and depth set to 70 µm. Points chosen per line and line per image were both set at 200. Scan speed [s/Line], retrace speed [s/Line], and integration time were set at 4.0, 0.50 and 0.02, respectively. High speed and low intensity setting were selected for carrying out fast scan utilising the EMCCD detector (1600 × 200 pixels). EMCCD gain was set at 230 and the preamplifier gain at 1. A 600 g/mm grating, laser wavelength of 532 nm and laser power of approximately 15 mw were utilised. The final setting parameter is the objective magnification which was set at 10x.

For the high temperature scans, an environmental stage purged with argon gas was utilised to modulate the temperature of a virgin sample whilst conducting the Raman scans. The objective was set at 50x, with depth scan area of 30 µm x 30 µm. Points chosen per line and line per image were both set at 100. Scan speed [s/Line], retrace speed [s/Line], and integration time were set at 5.0, 0.50 and 0.05, respectively. Laser power used was approximately 14mw, with the same laser wavelength and grating as above.

WiTEC project five plus software was utilised to process and analyse parts of the data. The cluster analysis feature was used to identify and distinguish different carbon signatures together with their respective locations mapped.

2.3. Kinetic analysis

The rate equation for solid state kinetic degradation process is expressed in Eq. (1)

$$\frac{d\alpha}{dt} = K(T).\ f(\alpha) \tag{1}$$

Where: da/dt is the rate of reaction (conversion rate) and $f(\alpha)$ is the mechanism of reaction. α- represents conversion obtained from the sample mass loss using the

Eq. (2). m_o refers to the initial mass of sample, m_t is the mass loss recorded at a specific time during degradation, and m_∞ is residual mass left behind after completion of test regime.

$$\alpha = \frac{m_o - m_t}{m_o - m_o} \tag{2}$$

K- represent the rate constant and can be derived from Eq. (3)

$$K\ (T) = A\ exp\frac{-Ea}{RT} \tag{3}$$

Eα- is the activation energy (KJ mol-1).
R- is the gas constant 8.314 JK-1.
T- is the absolute temperature measured in Kelvin.
A-is the pre-exponential factor (min-1).

In Eq. (3) K is dependant on temperature and is used to describe the general, non-isothermal case. Eq. (1) can now be transformed into the general, non-isothermal case by extension through a term dependant on temperature $\beta = (dT/dt)$ in Eq. (4). A keynote from a kinetic viewpoint is that α is a function of both time and temperature and a differential has been formulated to show that both time and temperature are independent variable expressed in Eq. (5) [36]. The β terms subsequently follows this differential

$$\frac{d\alpha}{dt} = \beta.\ \frac{d\alpha}{dT} \tag{4}$$

$$d\alpha = \left(\frac{\partial\alpha}{\partial t}\right)_t dT + \left(\frac{\partial\alpha}{\partial t}\right)_T dt \tag{5}$$

Eq. (6) is then formulated and serves as the basis for all non-isothermal kinetic reactions [36].

$$\frac{d\alpha}{dt} = \beta.\ \frac{d\alpha}{dT} = K(T).\ f(\alpha) = A.\ f(\alpha)\ e^{\frac{-Ea}{RT}} \tag{6}$$

2.3.1. Model free: isoconversion method

From Eq. (6) important isoconversion methods were derived [25,36–38]: Kissinger–Akahira–Sunose and Ozawa-Flynn-Wall methods respectively for Eq. (7) and 8.

Kissinger-Akahira-Sunose equation

$$\ln\left(\frac{\beta_i}{T^2_{\alpha,i}}\right) = ln\left(\frac{A_\alpha R}{g(\alpha)E_\alpha}\right) - \left(\frac{E_\alpha}{RT_{\alpha,i}}\right) \tag{7}$$

Ozawa-Flynn-Wall equation

$$\ln\beta_i = ln\frac{A_\alpha E_{\alpha,i}}{Rg(\alpha)} - 5.3308 - 1.052\left(\frac{E_{\alpha,i}}{RT_{\alpha,i}}\right) \tag{8}$$

The Arrhenius parameters can be obtained by plotting the first part of the equation against 1/T (α, i; as a function of conversion and heating rate) of the last part of the respective equations. From the slope of the graph and intersect, both apparent activation energy and pre-exponential factor/Arrhenius constant can be obtained. β denotes heating rate, α and i denote conversion and heating rate. Eq. (7, 8) are obtained from an integral form of an equation that relates to Eq. (6)'s derivative form depicted below [39]:

$$g(\alpha) = \int_0^\alpha \frac{d\alpha}{f(\alpha)} = \frac{A}{B}\int_0^T exp\left(\frac{-E}{RT}\right) = \frac{AE}{\beta R}p(x) \cong\ g(a)$$
$$= \frac{AE}{\beta R}\ e^{-x}\left[\left(\frac{1}{x}\right)^2 - 2!\left(\frac{1}{x}\right)^2 + 3!\left(\frac{1}{x}\right)^3 ..\right] \tag{9}$$

$$p\ (x) = \ e^{-x}\ \left(\frac{1}{x^2}\right) \tag{10}$$

The temperature integral p(x), where $x = E/RT$, has no analytical solution. Mathematical approximations were derived to enable derivation for Kissinger–Akahira–Sunose (KAS) and Ozawa-Flynn-Wall (OFW) methods. The Frank-Kameneskii approximation was used for the temperature integral approximation and had the values of x as "$20 < x < 50$"; which was used to derive the KAS equation [39]. To derive the OFW equation the Doyle's approximation was used, and it had values of x to be between "$20 < x < 60$" [19,38,39].

2.3.2. Non-Conversion method

The Kissinger and Ozawa are commonly employed techniques for determining a single activation energy for the entirety of the reaction. The Kissinger method is considered a limit law that obeys first order reaction model (f(α)=(1-α)) and it is often utilised to display the rate limiting step of a reaction according to Svoboda and Málek [36,40]. These methods were used to test the hypothesis of obtaining a predictive kinetic parameter that confirms their suitability in predicting either the initial rate or to evaluate whether its prediction corresponds to an extent of conversion (50%) as stipulated by N. Sbirrazzuoli et al. [41]. The equation for the Kissinger and Ozawa methods are below:

Kissinger equation

$$ln\left(\frac{\beta}{T_p^2}\right) = ln\left(\frac{AR}{E}\right) - \left(\frac{E}{R}\frac{1}{T_P}\right) \tag{11}$$

Ozawa equation

$$ln\beta_i = ln\frac{AE}{Rg(\alpha)} - 5.3308 - 1.052\left(\frac{E}{R}\frac{1}{T_P}\right) \tag{12}$$

From Eq. (12, 13) we can plot the first part of each equation against $1/T_{p,}$ with $T_{p,}$ denoting the maximum peak temperature from the DTG curve. These equations do not consider complexity of reaction mechanism by conversion.

3. Results and discussion

3.1. Non-Conversion method

The derivative thermogravimetric analysis (DTG) specifies the rate of percentage loss in weight due to oxidation of carbon as a function of temperature change (Fig. 2). The DTG peaks for each respective heating rates: 3 °C min^{-1}, 11 °C min^{-1} and 27 °C min^{-1} were distinctively shifted making it desirable for the application of model free kinetics. The peak temperatures of the DTG (T_p (K)) and heating rates (β) were used in plotting the Kissinger and Ozawa Plots as seen in Fig. 2.

From the thermogravimetric analysis (TGA) curve, there are two major stepwise drops in mass, owing to the different carbon types present within the composite namely: resin and graphite. The resin being a lower order carbon than graphite was expected to oxidise at a lower temperature, as indicated on the TGA curves (Fig. 1a).

The TGA data also shows the onset oxidation points of the variable heating programs used. The ability to delay the onset oxidation with faster heating rate is a useful point of measurement for end user application when heating these products. Industrials trials conducted by Svensson et al., has demonstrated that faster heating

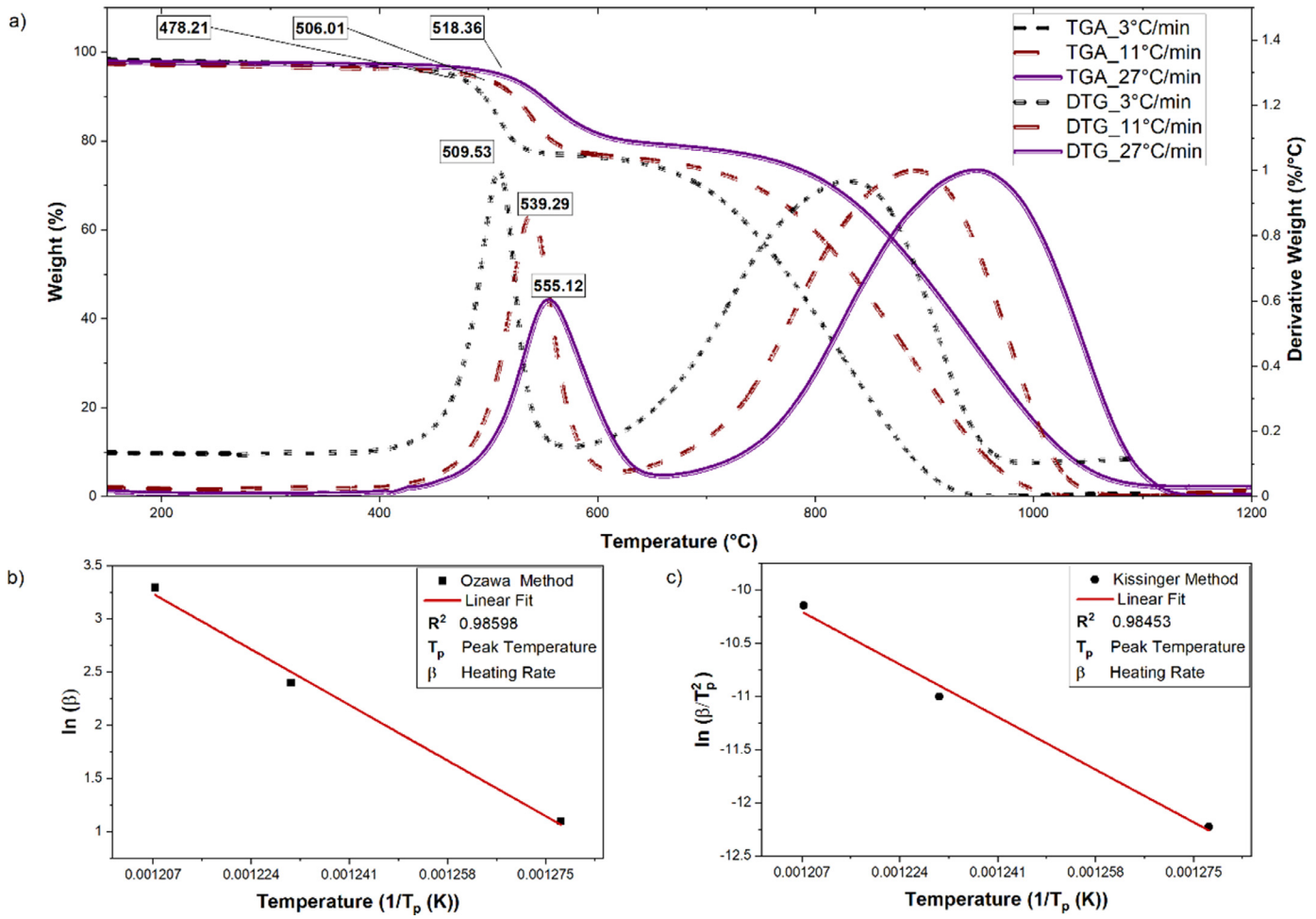

Fig. 1. a) Graph of weight change and its derivatives peaks showing resin and graphite oxidation within a carbon bonded refractory composite. b) Ozawa Arrhenius Plot c) Kissinger Arrhenius Plot.; β refers to heating rate and T_p refers to the peak temperature.

Table 1.
Shows the activation energy and Arrhenius parameter from both the Kissinger (α) and Ozawa (β) method employed. The symbol "(*)" refers to kinetic parameters obtained by equation method utilising heating rates; whereas the symbol "(Δ)" refers to parameters obtain from the intercept of the slope.

Ea	ln A	A
	$35.28_{(*)}$	$2.09E+15_{(*)}$
	$35.13_{(*)}$	$1.82E+15_{(*)}$
$242.11_{(\alpha)}$	$35.31_{(*)}$	$2.17E+15_{(*)}$
$242.84_{(\beta)}$	$40.34_{(\Delta)}$	$3.31E+17_{(\Delta)}$

rates were more effective in protecting the SEN against decarburisation and through the densification of silicon forming a glass protective coating upon activation at temperatures greater than 700 °C [12]. The effect of heating rate is also observed on DTG peak maximums otherwise known as the maximum mass loss rate. For the resin, there is a depreciation of the DTG as the heating rate increases indicating resistance to oxidation. The increase in heating rate is coupled with shift in temperature coverage of the DTG at higher temperatures caused by the accelerated heating of the sample exterior relative to its interior [42,43]. A study on the matrix graphite oxidation has shown low temperature oxidation to be more damaging through the preferential oxidation of resin-binder and mechanism of pore formation [44].

From the results obtained in Table 1., activation energy utilising both Kissinger and Ozawa method yielded equivalent values of activation energies; 242 KJ/mol. The slope of the graph in Fig. 1b, and 1c were used to calculate their respective activation energies. Both Kissinger and Ozawa method showed good linear fitting with high correlation coefficient indicated by R^2 value of 098,453 and 0.98598 respectively.

The Arrhenius constant for the Ozawa can be obtained directly from the intercept of the graphical slope with great confidence. However, an equation method based on variable heating rates was employed in deciphering the Arrhenius constant for the Kissinger (as opposed to utilising its intercept value). This equation can be found elsewhere for reference (xu et al., curing study) [45]. Nevertheless, the Kissinger's intercept value for the Arrhenius constant was compared against those obtained from the equation-based method and with respect to Ozawa. The order of magnitude difference between the Arrhenius constants from both Kissinger and Ozawa decreased from 7 to 2; once the equation method was applied to Kissinger. This may imply an improvement in Kissinger's prediction with the use of the equation-based method.

To further evaluate the differences in Arrhenius constants, between the two methods; their rate K (T) constants were calculated using Eq. (3) for each respective method. The kinetic parameters of activation energy and Arrhenius constant obtained from both Ozawa and Kissinger served as inputs variables into Eq. (3). Three respective temperatures were tested at: 510 °C, 540 °C and 570 °C. Isothermal experiments for validation using the same temperatures as above were also conducted. The choice of temperatures helped

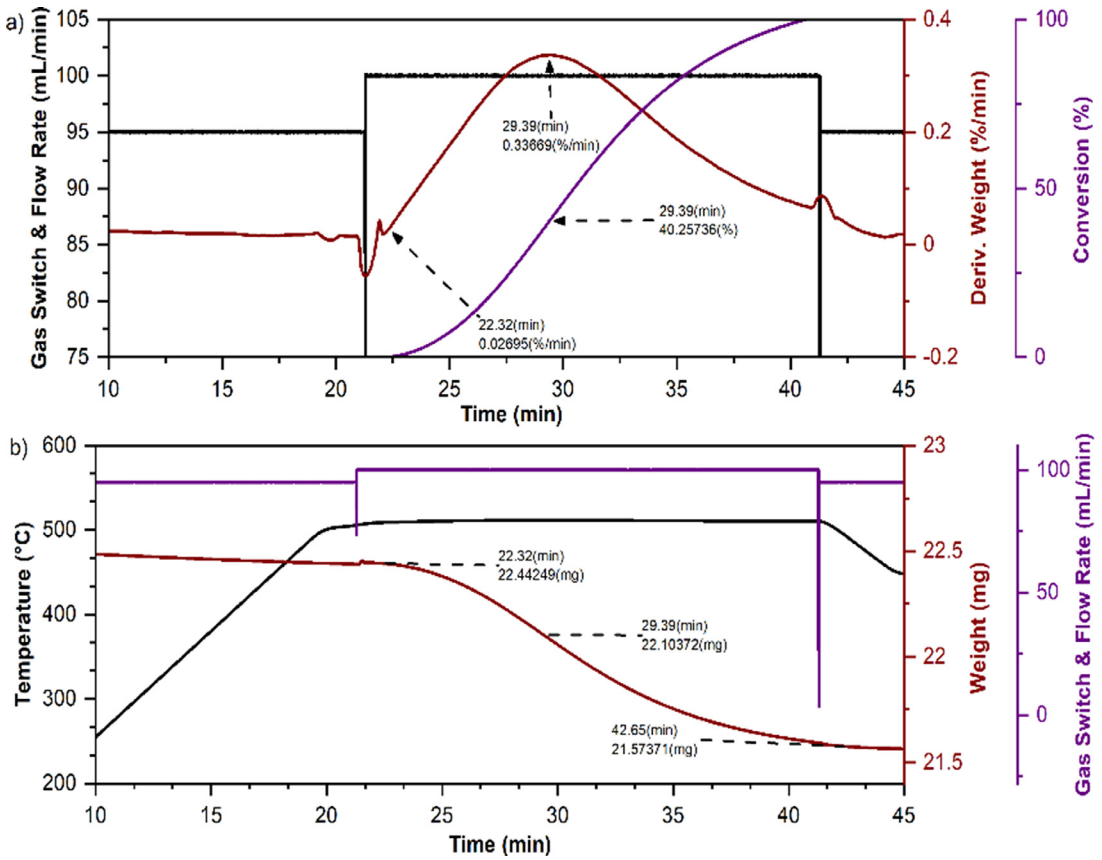

Fig. 2. a) Shows the derivate of mass loss (brown line) against time in the isothermal experiment at 510 °C; initiating 22.3 min after the gas flow was changed from an inert to an oxidising environment. The purple line depicts the percentage conversion occurrence. 40% conversion is equivalent to the peak maximum derivative. b) The TGA plot of mass loss (brown line) against time, with gas switch depicted in purple and temperature program in black.

clarify predictions with respect to initial rate and/or peak maximum rate at these temperatures.

Experimentally measured maximum peak derivatives were: 0.3367%/min, 0.3675%/min, and 0.4637%/min for each of the respective temperatures (°C) at 510, 540 and 570. The predictive rates for the Kissinger were too low (∼ 0.0025%/min for 510 °C) and therefore considered inaccurate in terms of predicting initial rate or peak maximum derivative/rate.

The Ozawa predicted rate constants were: 0.30575%/min, 0.54875%/min, 0.7915%/min for each respective temperature (°C) at: 510, 540 and 570. The closest agreement of rate prediction with respect to isothermal experiment was with 510 °C. It is therefore reasonable to infer that the kinetic parameters obtained from Ozawa can be used for predicting maximum derivatives but within a small temperature region from its onset (487 °C −510 °C).

Fig. 2. shows the rate at peak maximum of the isothermal experiment which is in close agreement with Ozawa's prediction at 510 °C. The initial rate can also be observed in Fig. 2; it was approximately 0.027%/min and extrapolated at 0.1% conversion from the start of oxidation. The initial rate value was not predicted by either of the methods employed.

It is key to note that these methods cannot be used to decipher complexities of reaction mechanism as they only produce a single averaged kinetic parameter for the entirety of the reaction, as opposed to the isoconversion methods.

3.2. Model free (Dynamic model) isoconversion

3.2.1. Evaluation of Ea with respect to Ln A

The isoconversion method allows the determination of complexities in reaction kinetics, by providing the kinetic parameters as a function of conversion. Clear differences were observed in the activation energy and Arrhenius constant values obtained for both OFW and KAS methods. Overall, the KAS method predicted higher kinetic parameters than the OFW method (See Fig. 3d). However, the descending trend of values obtained were similar. To test the reliability of the methods used in predicting these values, the temperature integral limit of 'x' was assessed for both KAS ($20 < x < 50$) and OFW ($20 < x < 60$); using $x = Ea/RT$ (where Ea, is the activation energy and T is the average temperature from the isoconversion plot). The OFW was found to be more accurate than the KAS, based on its values of 'x', staying within the approximation limit (Supporting information: Figure S2) KAS method was not further analysed as result.

Both activation energy and Arrhenius constant decrease as a function of temperature shift and conversion (Table 2). In simple reactions, the decrease in activation energy is associated with an increase in rate where the change in Arrhenius constant is not significant. However, observations from the experimental data shows rate/derivative to increase steadily and peaks at 60% conversion before decreasing. The effect of Arrhenius constant was therefore included in the analysis to understand the reaction behaviour.

The effect of Arrhenius constant can be explored by its association with entropy. By utilising the rate dependency of the activated complex theory approach; the equilibrium shift between the reactants and activated complex formed can be studied from a thermodynamic perspective using the Gibbs free energy equation:

$$\Delta G = \Delta H - T\Delta S \tag{16}$$

Where, an increase in entropy (ΔS) lowers the Gibbs free energy (ΔG), shifting the equilibrium towards forming more of the acti-

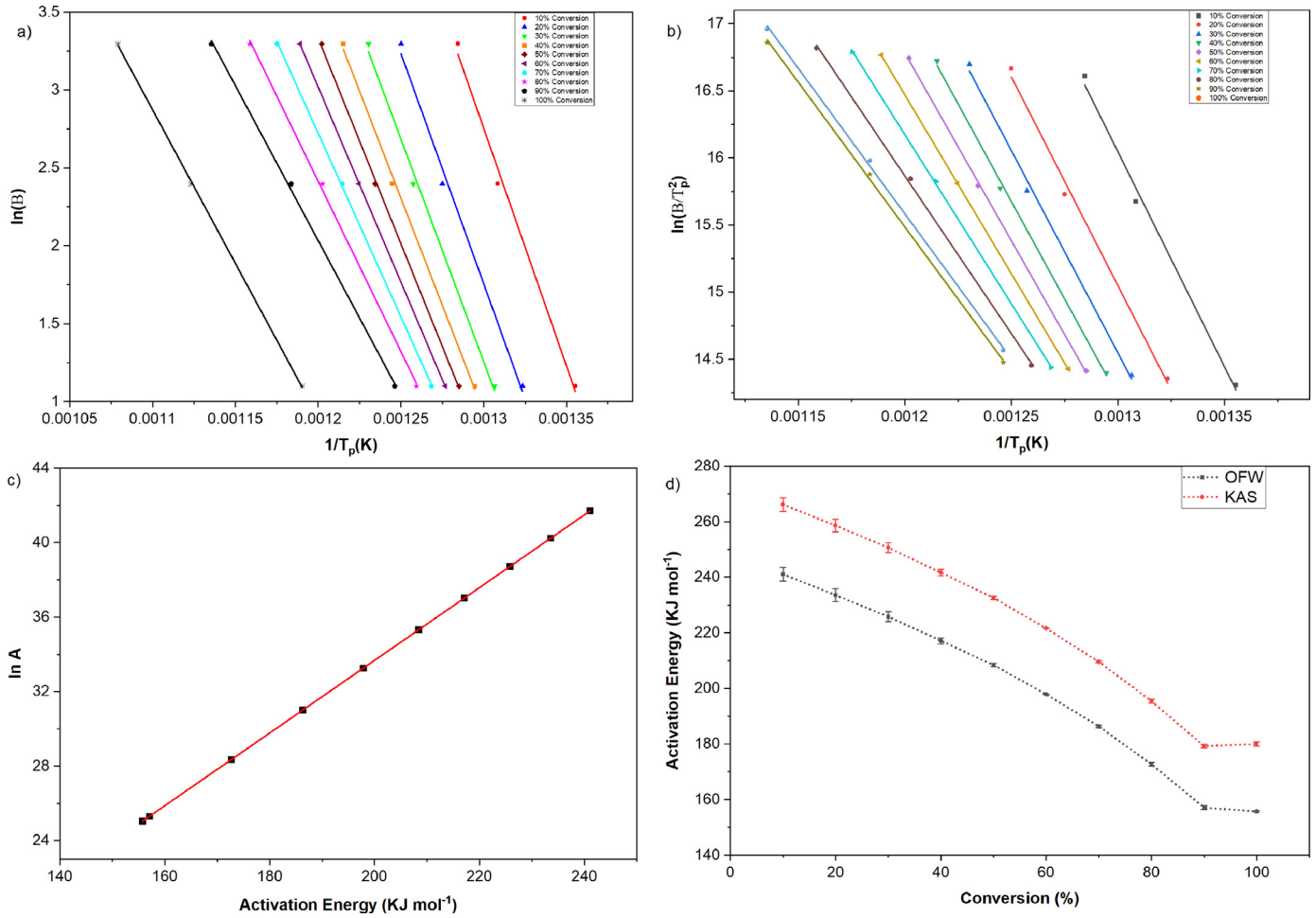

Fig. 3. The Arrhenius plots of the a) OFW method and b) KAS method; showing respective conversions fitted with linear regression analysis, with the slope and the intercept of each corresponding to the activation energy and Arrhenius constant respectively. c) Plot of the compensation effect showing the linear relationship between ln A against activation energy. d) Activation energy as a function conversion for both OFW and KAS (KAS overprediction of kinetic parameters).

Table 2
Kinetic parameters for the isoconversion method: Ozawa Flynn Method. "*" indicates the "ln A" parameter has been adjusted through the compensation effect.

OZAWA-FLYNN WALL METHOD			
Conversion (%)	Ea (KJ mol^{-1})	R^2	* lnA
10	241.1 ± 2.5	0.98699	52.4 ± 3.3
20	233.6 ± 2.3	0.98804	51.0 ± 2.9
30	225.8 ± 1.8	0.99248	49.4 ± 2.2
40	217.1 ± 1.1	0.99662	47.7 ± 1.4
50	208.4 ± 0.6	0.99902	46.0 ± 0.7
60	197.9 ± 0.1	0.99998	44.0 ± 0.1
70	186.3 ± 0.4	0.99947	41.7 ± 0.5
80	172.7 ± 0.7	0.99782	39.1 ± 0.9
90	157.1 ± 0.6	0.99814	36.0 ± 0.7
100	155.8 ± 0.7	0.99959	35.8 ± 0.3

vated complex. The total entropy ΔS is a factor consisting of the difference in entropy of reactants to that of the activated complex (entropy of activated complex). The calculation of entropy can be obtained by the following:

$$A = \frac{k_\beta T}{h} \exp\left(\frac{\Delta S}{R}\right) \tag{17}$$

$$AS = R \ln\left(\frac{\Delta h}{k_\beta T}\right) \tag{18}$$

The above equation is taken from rate dependency relationship of the activated complex theory (with substitution of ΔH to Ea one can relate this to Eq. (3) of the Arrhenius rate Eq. (3)):

$$A = \frac{k_\beta T}{h} \exp\left(\frac{\Delta S}{R}\right) \exp\left(\frac{\Delta H}{RT}\right) \tag{19}$$

Where, k_β, h and ΔH are the Boltzmann constant, Planck constant and enthalpy change respectively.

It is observable from the relationship that the value of entropy is highest at the beginning of the reaction and decreased as reaction progressed (see Fig. 4). It has been noted by Luchini et al., that thermal expansion mismatch is known manifest itself significantly at temperatures around 500 °C causing pore closure, densification, and a rise in the elastic young's modulus of the material [46]. Werner et al., also found the same trend in their study quoting an initial temperature of 400 °C; and stating that this onset temperature depends on carbon content and grain size (i.e., composition based) [47]. It was also noted that the alumina and the graphite phase are more affected by temperature increase above this temperature due to their higher thermal expansion coefficient than the glassy carbon/resin [46,47]. It is therefore feasible to extrapolate that pore closure restricts mobility of the activated complex formed when entropy decreases but this can only be held true when the entropy change is positive. Oxidation of carbon is a dissociative process.

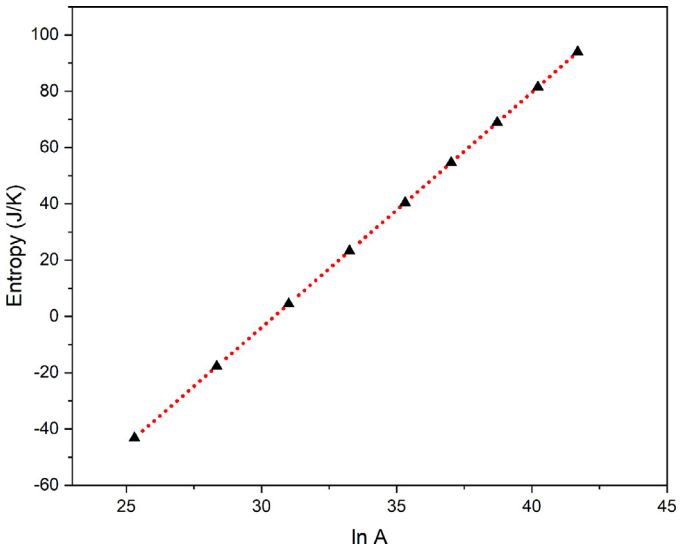

Fig. 4. Graph of Entropy change against ln A showing linear decrease of entropy as a function the Arrhenius constant.

Theoretically, decreasing the total entropy change of activation, (when positive) means that there is a decrease in the gap between activation entropy of reactant and activation entropy of activated complex [48]. As explained by Vyazovkin [48] this is achievable by either increasing activation entropy of reactants or decreasing the activation entropy of the activated complex. In this case it is the latter.

The entropy takes on negative values (associative process) as the reaction nears the end (refer to Fig. 4). From the Raman data, orderliness of carbon phase was observed on the surface as temperature increased (refer to Fig. 8). Additionally, pore closure is expected to increase as temperature increases causing further densification and expansion of graphitic phase [46]. Therefore, the increase in entropy in this case (i.e., becoming more negative) is due to the lowering of the activation entropy of the reactant. This is to be expected as pore closure should restrict molecular mobility which is also supported by the orderliness observed by the Raman data (refer to Fig. 8).

Theoretically, an increase in entropy (i.e., becoming more negative) due to pore closure reduces the gap between the activation entropy of activated complex and activation entropy of reactant [48]. This is achievable by lowering either the activation entropy of reactant or increasing the activation entropy of activated complex [48]. In this instance, it is the former.

3.2.2. Isothermal predictions and reaction complexity

Isothermal predictions were attempted and evaluated against isothermal experiments at temperatures (°C):510, 540 and 570. By utilising a the Friedmann approach the time taken to reach a set conversion is possible to calculate from a model free perspective using the equation below (t_α = time taken, T= temperature, α = conversion, f(α) is the reaction model):

$$t_\alpha = \int_0^t dt = \int_0^\alpha \left[\frac{d\alpha}{A_\alpha \ f(\alpha) \exp\left(\frac{-E_\alpha}{RT_\alpha(t)}\right)} \right] \quad (20)$$

However, due to the complexity of reaction mechanism and inadequacies in the predicted kinetic parameters of the OFW method (in terms of accuracy), the isothermal prediction with the Friedmann derived method proved difficult to achieve when used in the conventional manner i.e., it did not produce values comparable to the isothermal experimental data when trialled.

To overcome this issue, the Vyazovkin activation energy was used in place of OFW. The vyazovkin method is known to be more accurate in predicting complex reactions [27,49]. Vyazovkin activation energy was obtained with software created by Drozen et al., [49] (Supporting information: Table S1). The Arrhenius constants were calculated using the OFW compensation constants “a” and “b” as they produced the best predictions.

Additionally, a modified empirical approach was determined using the same equation above (Friedmann derived) but with carefully selected combinations of kinetic parameters as inputs, at set temperatures. These kinetic combinations (Ea and A) produced a linear graphical trend with the same R^2 value of 0.983 (see Fig. 5a). The linear regression equations from the graph were subsequently used to calculate the time taken predictions.

Three kinetic input parameters of Ea and A were taken from conversions of: 60% (peak maximum), 70% and 80%. Three average temperatures from the non-isothermal runs corresponding to: 10% conversion (487 °C), 20% conversion (506 °C), and 60% conversion (540 °C), were also selected to correspond with the kinetic parameters, respectively. Finally, the reaction model f(α) was kept the same for all three calculations and selected at 20% conversion. The reaction model of f(α) was calculated in a model free approach found. These combinations provided the best fitting for the predictions.

For each respective conversion, the predictions for the time taken reduced as a function of temperature increase. A subtle difference was noticed when compared to experimental isothermal data in terms of trend. The time taken to reach the same set of conversion also reduced as a function of each incrementally tested temperature (510 °C, 540 °C and 570 °C) but with an anomaly at 570 °C. This anomaly is indicative of the complexity in the reaction mechanism especially at higher temperatures. The time taken seemingly increased (i.e., loses trend) at this temperature but only for conversion less than 50% (refer to Fig. 5b). Conversion at 50% and beyond did decrease to follow the trend however, this decrease was very marginal when compared the previous temperature (refer to Fig. 5b). This would suggest that at higher temperatures pore closure has a greater effect causing a slight delay in the overall reaction.

The accuracy of the isothermal prediction was dependant on both conversion and selected temperature of interest (See Fig. 5c and 5d). The predictions seem to work best at lower temperatures less than 510 °C. By setting a standard error baseline of $<$ 0.5, a good prediction is achievable for 40% to 80% conversion with respect to 510 °C (See Fig. 5). If 540 °C was to be used, then a good prediction can also be obtained with conversion 50% to 80% whilst maintaining the same error threshold of $<$0.5. It is not advisable to use the prediction for 570 °C due to margins of error being too high. The complexity of reaction is more pronounced at higher temperatures as depicted on Fig. 5b, (reaction rate fails to decrease entirely as a function of temperature) making the isothermal prediction unsuitable beyond 540 °C.

These results were also assessed against common solid-state kinetic models to see if there is mechanistic fit. From the models tested, no overall fitting was observed owing to the complexity of reaction mechanism as previously noted. However, the agreement in terms of the explanation for what was observed with the isothermal predictions was coherent. At lower conversions of 20% (equivalent to average temperature of 506 °C) and less, there is a possible fit (cross-over) with certain nucleation models and power-based models. The avrami models of A4 and A3 and the power model of P4 showed the best agreement at 10% conversions or equivalent averaged temperatures (Supporting information: Figure S3). At 20% conversion F3 (third order) and A4 model (avrami) showed the best agreement. The agreement at these lower conversions could prove why the isothermal predictions only works

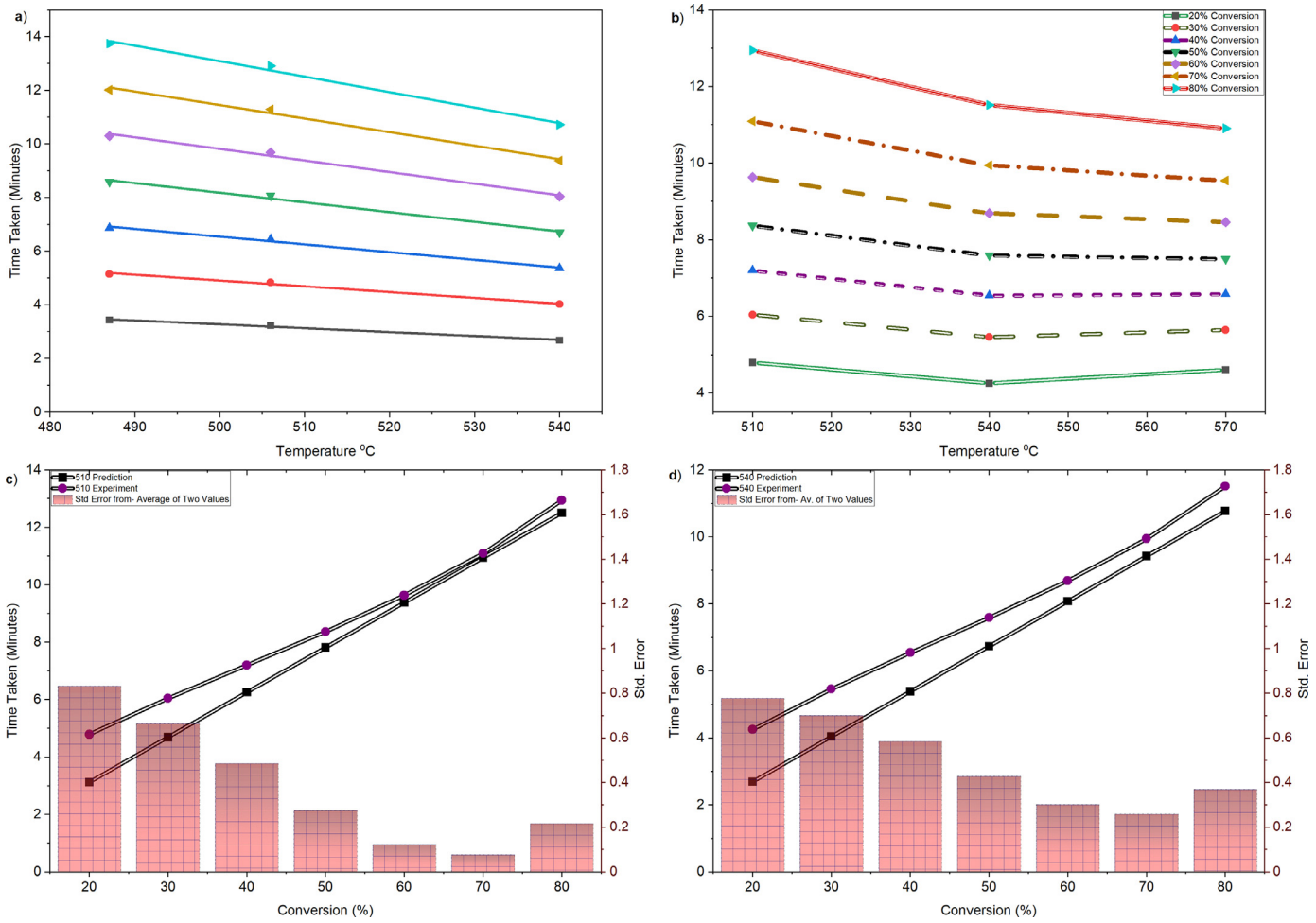

Fig. 5. a) Empirical model of Time taken to reach a conversion point vs Temperature. The model was built using three selected kinetic parameters fitted with a linear regression whose equations are used for predicting isothermal experiments. b) Time taken isothermal plots of experimental data at 510, 540, and 570 showing the downward or upward trend at these temperatures. c) Isothermal prediction for 510 compared against experimental value. d) Isothermal prediction for 540 compared against experimental value; standard error plots showing degree of difference.

best at lower temperatures. From the z(a) master plots, the curve of the experimental plot followed a mixture of avrami and exponential/power law in terms of trend but never quite fits any of the models due to its complexity and varies drastically as temperature/conversion increased (Supporting information: Figure S3). This observation demonstrates that whilst theoretically useful, such approaches have limited practical value in industrial applications in the current context and reinforces the requirement for more rapid characterisation and assessment tools such as those presented herein.

3.3. Raman analysis

3.3.1. Tracking oxidation

Raman spectra was acquired for four incrementally oxidised samples at with 1 min interval apart. Only the resin was oxidised during this experiment. This was achieved by setting the isothermal temperature for oxidation at 510 °C, which was below the oxidation temperature of the graphite. Samples were oxidised in bulk form to capture the effect of microstructure which was also the case for the kinetic derivation of the reactions above.

The cluster algorithm of the WiTec software was used to separate out or distinguish between carbons and carbons signals affected by substrates. Locations of both graphite and resin were clearly mapped and organised in clusters based on features of resemblance. Each scanned region was divided up into 4 clusters. The cluster that was least affected by aggregate or substrate effects in each scanned region was used in determining the oxidation relationship. A single Lorentzian fitting of the G and D peaks were used in these calculations by way of deconvolution fitting recommendation extrapolated from Mallet-Ladeira et al., study [50].

The Raman vibrational modes detected were mainly the G peak, D peak and 2D peaks as illustrated on Fig. 6. The G peak in Raman arises due to vibrations of sp2 bonding (pi-bonds) found in aromatic or graphitic type compounds [51,52]. Structural ordering of carbons and nano-crystallite size can be determined from the G peak [52]. In terms of crystallite size calculations, the proposed method by P. Mallet-Ladeira et al., was utilised for the resin whilst the method proposed by Maslova et al., was applied for the graphite [50,52]. In literature, the G-peak shift is normally recorded as 1580 cm^{-1} (in the case of perfect graphite with no residual stress) whereas the D peak is recorded at approximately 1350 cm^{-1} and is referred to as a disorder induced mode which is absent in defect free graphite [52–54]. The intensity of the D peak becomes more pronounced as the graphitic compounds becomes less ordered or more defective.

Fig. 6., shows a typical depth scan with only a single cluster shown (i.e., the cluster least affected by substrate effects such as aggregates within the composite) and masking the others. The

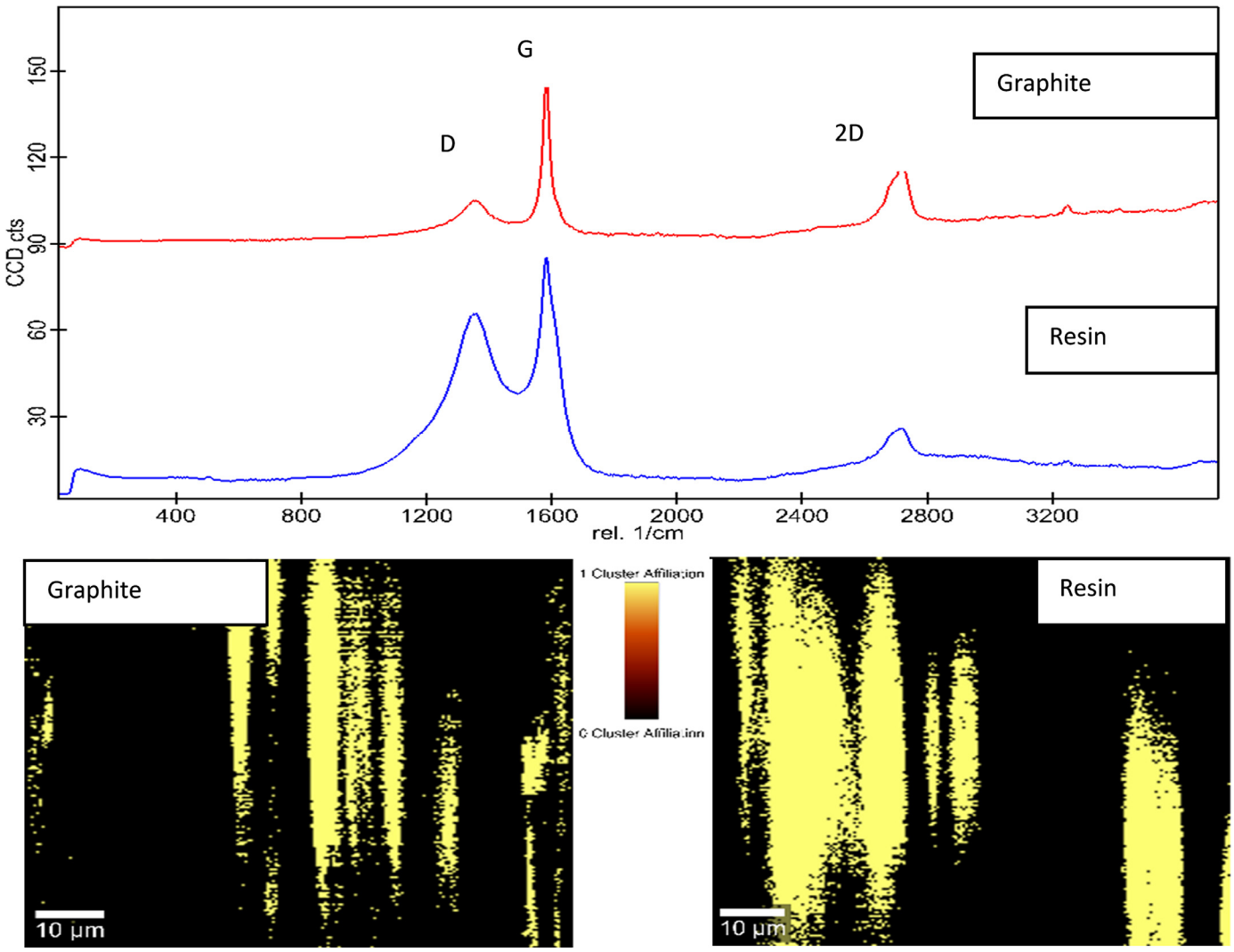

Fig. 6. Cluster analysis showing depth scan of carbon components with their respective locations mapped (in yellow). Graphite spectra on the top (red) and resin spectra on the bottom (blue). The masked feature of the Raman imaging software is used to indicate the locations of both resin and graphite by hiding one (black region of map) and exposing the other (yellow region of map).

commonly used intensity peak ratio of G to D peak (useful for determining how ordered or defective the carbons are), and crystallite sizes were evaluated as a function of oxidation [24,52,55]. The intensity ratios of both the graphite signal and resin decreased as a function of oxidation with a slight anomaly for the resin cluster (See Fig. 7c and 7d). The decreased in trend as a function of oxidation only holds true from the start of oxidation to 3 min oxidation timepoint (approximately 20% resin conversion). Beyond this point (i.e., at 4 min timepoint), the level of partial oxidation within the bulk sample is considered too high in that the Raman cluster signals obtained were greatly affected by the substrate effects within the bulk (Supporting information: Figure S4). These results indicate that there is a limit to the extent at which resin clusters can be traced with confidence during the partial oxidation process. The graphite cluster signals were also affected by the substrates within the composite at this stage but to a lesser degree and therefore maintained trend (refer to Fig. 7d).

A similar effect was also observed on the measured crystallite sizes at the 4-minute interval point for the resin cluster (See Fig. 7a) where the trend was lost at this point. However, the crystallite size generally increased as a function of oxidation for the resin cluster. The graphite crystallite size did not change much with respect to resin oxidation but exhibited an anomaly at 3-minute oxidation time-point (See Fig. 7b), which can be attributed to the fitting method employed [50] and substrate effects [55].

Lu, et al., traced oxidation of nuclear graphite utilising Raman but only found a trend with oxidation using FWHM (full width half maximum) of the G peak [24]. Accordingly, it was found that progressive oxidation decreased the FWHM of the G peak [24]. It was inferred in their study that oxidation can be tracked by monitoring the preferential oxidation of binders (i.e., with smaller nanocrystallite size) exposing filler particles (i.e., with larger nanocrystallite). This would lead to an increase of observable nano-crystallite sizes as samples are oxidised which confirms the trend observed in this work.

Moreover, Lu et al., did not find any trend with regards to the intensity ratio of the G to D peak [24]. However, a further assessment of peak components of the resin cluster within this showed a decrease in trend with intensity ratio; that is if we excluded the timepoint at 4 min due to signal interference. The graphite, however, did not show any trend with regards to intensity ratio due substrate effects. In fact, it is important to also note that graphite was not oxidised in this study as it was in Lu et al., study [24]. Moreover, individual peak intensities of the G and D peak decrease in trend with respect to oxidation for the resin cluster if we exclude time-point at 4 min.

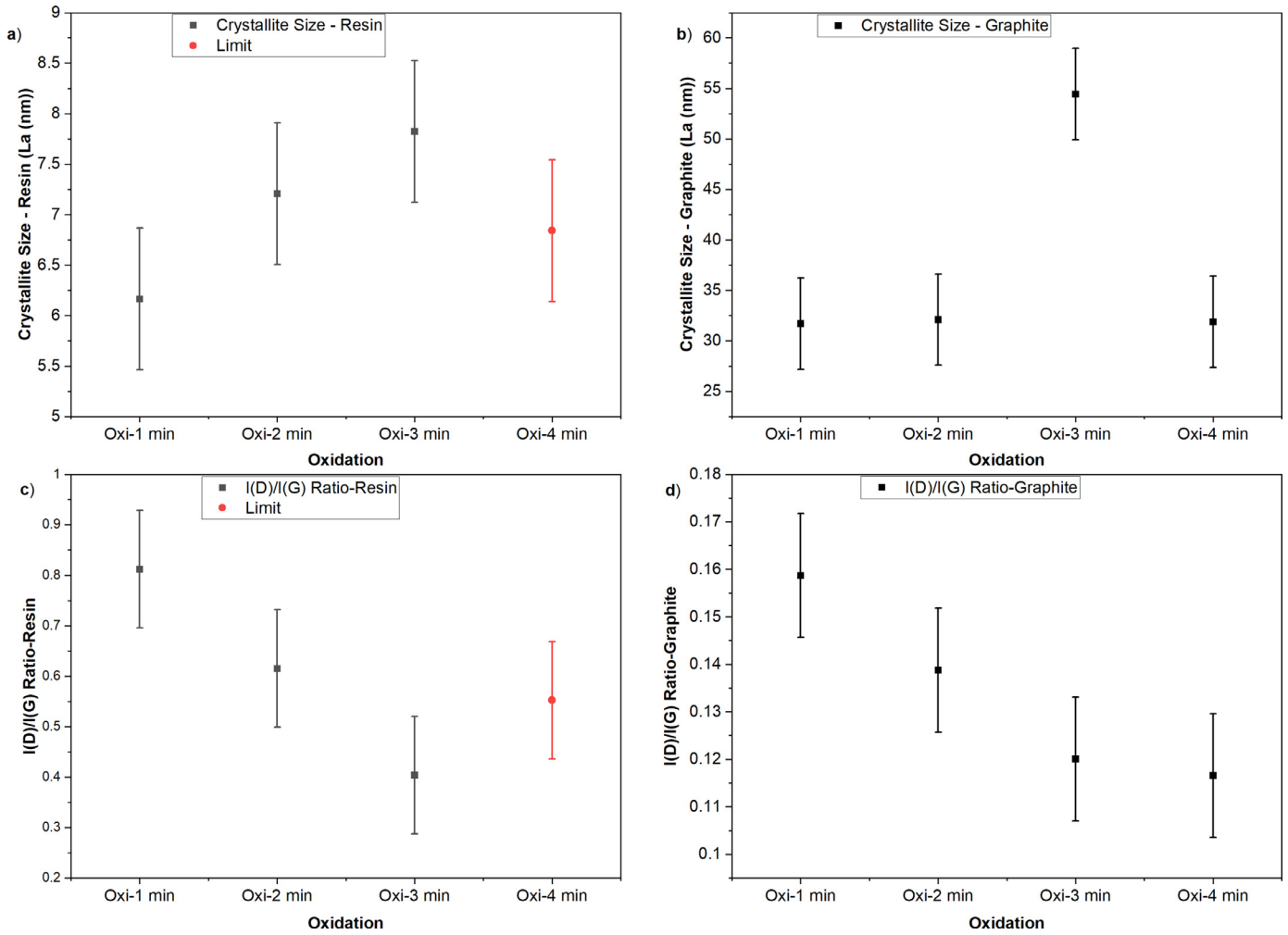

Fig. 7. a) Changes in crystallite sizes of resin cluster as a function oxidation time with limitation noted where the trend is lost. b) Graphite crystallite size remaining constant with the exception at 3-minute interval oxidation timepoint. c) Resin cluster intensity ratio of D to G peak downward trend with oxidation and its limitation on oxidation time point at 4-minute d) Graphite cluster intensity ratio of D to G peak downward trend with oxidation.

There was an expectation that the G intensity of graphite may increase as the resin oxides. However, this was not the case due to signal interference at the two-minute interval. The G intensity signal was suppressed and therefore decreased, before increasing again at the 3 min and 4-minute interval. Depth scan spectra at the 2 min oxidation timepoint showed evidence of high intensity TiO_2 signals, accompanied with a considerable reduction of the G and D peak of both resin and graphite clusters. This would suggest that a critical amount of resin and aggregate could have a significant signal interference. We can also deduct from studies aimed at improving the photocatalytic behaviour of titania that an increased amount of titania on the surface often decrease the graphene signal and vice versa [56–58]. Clear peaks of titania were identified at 158, 399, 501 and 615 (rel.cm^{-1}) and were noticeable during the scan at 2 min oxidation (Supporting information: Figure S5) [56–58].

To assess the influence of alumina which is the major aggregate in the composite material. Changes of peaks components were assessed for both the resin and graphite cluster at the 4- minute interval point and compared against 3-minute oxidation timepoint. For the graphite cluster, the G peak intensity seems to be most affected component (amplified/increased) whilst the rest of its components remain relative stable (Supporting information: Figure S4). This stability is the reason why it can be used to track oxidation all the way to the 4-minute time point

For the resin clusters only the hwhm (half width half maximum) of the G peak remained slightly stable, however the rest of the peak components increased significantly due to the effect of alumina. The changes observable with resin components may be due to several reasons including: the amount of resin left post oxidation, and the poor suppression of the fluorescence effect of alumina (which increases in amount as a function of oxidation) compared to graphite or graphene compounds [59]. Dielectrics such as alumina can amplify Raman signals through a process of interference [59].

During oxidation, the G-peak position shifted indicating strain effects experienced by the remaining carbonaceous matrix. Shifting of the G-peak to lower values were observed from initial oxidation to the 3-minute timepoint - for the resin clusters (1586 rel.cm^{-1};1582 rel.cm^{-1}; 1579 rel.cm^{-1}). This implied that the compressive state of the resin clusters changed as a function of oxidation at room temperature. The graphite G peak position changed only at the 3-minute and 4-minute oxidation point, indicative of both substrate effect and fitting method employed as previously stated. The graphite cluster transformed into a tensile state at the 4-oxidation timepoint (1576 rel.cm^{-1}).

3.3.2. High temperature microstructural evaluation

Temperature modulated depth scans were conducted on a virgin sample to study the microstructural influence that could im-

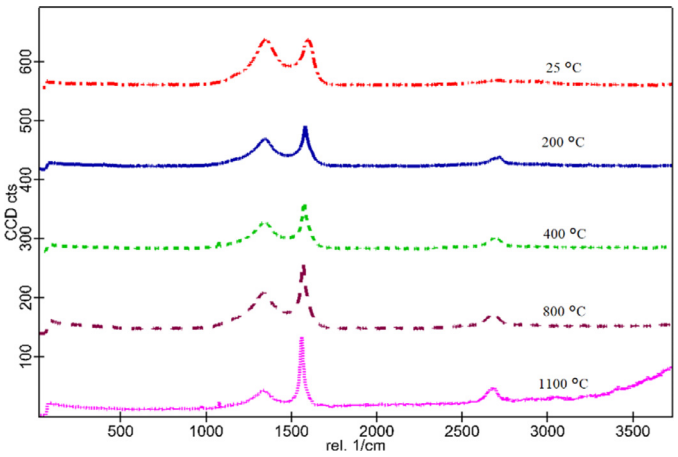

Fig. 8. Resin cluster least affected by substrates, scanned as function of temperature. The reduction D peaks and increase of the 2D peak resolution is indicative of the influence of graphite and microstructural changes limiting the visibility of resin structure.

pact on the kinetics of oxidation, or the complexity of reaction observed. The strain states of the carbons were investigated as function of the following temperatures (°C): 25, 200, 400, 600, 800, and 1100). An increase in shift/position of the G-peak from its normal position of 1580 cm-1 is indicative of compressive strain and a decrease from the same position implies a tensile strain [53,54]. To obtain the G-peaks positions reliably a single lorentzian fitting was used to fit onto the peak with the aid of WiTec software.

Cluster analysis was also employed to distinguish between carbons affected by substrates/aggregates to those least affected. A resin rich dominant region was scanned as a function of temperature and compared against a graphite dominant region. Each region was divided up into three clusters, two of which were highly influenced by aggregates within the composite; leaving only one cluster that was the least affected for both the resin and graphite dominant regions.

For the resin dominant region, the cluster that was least affected by aggregates changed from a compressive state (1587.88 rel.cm^{-1}) at 25 °C to a tensile state (1578.06 rel.cm^{-1}) at 200 °C (refer to Fig. 8 and supplementary: Table S2). This is in contrast to the graphite dominant region which transitioned from compressive to tensile only at 400 °C (1578.06 rel.cm^{-1}). The two remaining clusters for the resin dominant region all followed a similar trend to the graphite above. These clusters (resin) that were highly influence by aggregates were also in a more compressive state at 25 °C than the cluster of resin that was least affected by substrates effects. The remaining two clusters for the graphite dominant region also followed (almost identical) the same trend to the graphite cluster that was least affected by substrates. Refer to the supplementary: Table S2 for values of fitting respective clusters.

What was unique about these findings is that the visibility of the resin cluster that was least affected by substrates diminished as function of temperature. There was a noticeable increase in the 2D peak and reduction of the D peak. These observation points to microstructural changes of orderliness with regards to carbon and the graphitic influence (i.e., expansions) as temperature increased. The severe reduction of the D-peak at 1100 °C (i.e., mainly graphite that is detected) could be as a result of resin pyrolysis coupled with the pore closure mechanism.

With the exception of the resin cluster that was least affect by substrate (supplementary: Table S2); the change in strain state from compressive to tensile at 400 °C for all other clusters confirms the microstructural influence with much emphasis on aggregates and graphite interaction. This can be used as an indicator or point to focus on in terms detecting where (i.e., temperature) the possible thermal expansion mismatch lies that governs pore closure mechanism explained by Luchini et al., and Werner et al., [37,50]. Densification and pore closure of the carbon matrix is expected at critical temperatures where thermal expansion mismatch between aggregate and graphite is significant to cause a sudden increase in the elastic modulus of the material. The clusters with significantly influenced by aggregate together with the graphite rich region all point to this critical temperature of 400 °C. The ability to measure the strain state in Raman using carbon as a sensor provides the unique tool to trace this temperature in conjunction with monitoring the surface carbon characteristics of resin rich region to visualise microstructural changes governing the kinetics and thermodynamic of oxidation behaviour.

4. Conclusion

Oxidative degradation behaviour of resin within a carbon-based refractory composite was successfully studied in bulk material using model free kinetics and Raman spectroscopy.

Activation values ranged for the isoconversion methods ranged between 241 KJ/Mol to 155 KJ/Mol for OFW and 230 KJ/Mol to 150 KJ/Mol for Vyazovkin. The activation energy for Ozawa and Kissinger were both 242 KJ/Mol, for the non-conversion-based method.

The non-conversion method of Ozawa can be used for predicting initial rate at the initial onset temperatures below 510 °C. The predicted rates would correspond to the peak maximum rate at the investigated temperature.

Multi-step reaction behaviour was studied effectively using the isoconversion method, supported by theoretical thermodynamics and complimentary Raman data highlighting microstructural changes governing the reaction kinetics. The pore closure due to thermal expansion mismatch is a key feature slowing the reaction as a function of incremental temperature change. The different strain states within composite may add to the complexity of reaction depending on the region exposed.

Prediction of isothermal experiment which is seldom reported in complex reaction from a model free perspective was successfully conducted using an empirical graphical approach. Prediction works best at lower temperatures below 510 °C. If used to predicted temperatures slightly above, then consideration must be placed on the region of conversion that gives the most reliable results. It advisable to not use this approach for temperatures beyond 540 °C according to the experimental results. It is key to note that this parameter may be useful when determining the life of carbon for cases where under heating/improper preheating is suspected by steel end-user.

Tracing oxidation with Raman peak intensity ratio and crystallite size was proved possible but with limitations of use depending on the amounts of total resin lost (20% conversions) and substrate effects from certain aggregates such as alumina and titania known to amplify or suppressed signals respectively.

In future, an investigation into the microstructural features of pore formation upon oxidation will be great use to understand the difference between small partial oxidation observed at low temperatures in this study compared to oxidation at high temperatures where degradation of graphite is also established.

From a metallurgical perspective, these profiling tools would also provide a means to rapidly benchmark and investigate process influences (i.e., preheat time and adjustment of burner alignment) on the performance of their product (i.e., the SEN in this case). They can be used to potentially trace microstructural changes resulting from the process of preheating, profiling the resistance to oxidation as a function of preheat time or even detecting microstructural changes due to minute levels of oxidation that may

occurs in service, a capability which does not currently exist in this context.

Declaration of Competing Interest

We would like to declare that there is no conflict of interest.

Acknowledgement

The research used UKAEA's Materials Research Facility, which has been funded by and is part of the UK's National Nuclear User Facility and Henry Royce Institute for Advanced Materials.

We wish to acknowledge the support of the Henry Royce Institute for (**E.S**) through the Royce PhD Equipment Access Scheme enabling access to High Temperature set up of their WiTec Raman CSLM facilities at Royce@UKAEA-CCFE; EPSRC Grant Number EP/R00661X/1).

We wish to acknowledge our sponsors: Materials and Manufacturing Academy (M2A) funded by the European Social Fund and TATA Steel UK (Port Talbot); and sponsor company members Dr Liam Way (TATA Steel) and Mathew C Davies Way (TATA Steel) and the SUSTAIN EPSRC Future Steel manufacturing Research Hub (EP/S018107/1).

Supplementary materials

Supplementary material associated with this article can be found, in the online version, at doi:10.1016/j.cartre.2022.100174.

References

[1] L. Pilato, Phenolic resins: a century of progress, Phenolic Resins: A Century of Progress (2010) 503–515, doi:10.1007/978-3-642-04714-5.
[2] J. Poirier, A review: influence of refractories on steel quality, Metallurg. Res. Tech. 112 (2015) 410, doi:10.1051/metal/2015028.
[3] E.M.M. Ewais, Carbon based refractories, J. Ceram. Soc. Jpn. 112 (2004) 517–532, doi:10.2109/jcersj.112.517.
[4] A.P. Luz, R. Salomão, C.S. Bitencourt, C.G. Renda, A.A. Lucas, C.G. Aneziris, V.C. Pandolfelli, Thermosetting resins for carbon-containing refractories: theoretical basis and novel insights,, Open Ceramics 3 (2020) 100025, doi:10.1016/j.oceram.2020.100025.
[5] K. Sugita, Historical overview of refractory technology in the steel industry, Nippon Steel Tech. Rep. 98 (2008) 8–17.
[6] S. Banerjee, Iron and steel making refractories, Trans. Indian Ceram. Soc. 60 (2001) 115–120, doi:10.1080/0371750X.2001.10799983.
[7] L. Zhang, J. Zhi, F. Mei, L. Zhu, X. Jiang, J. Shen, J. Cui, K. Cai, B.G. Thomas, Basic oxygen furnace based steelmaking processes and cleanliness control at Baosteel, Ironmaking & Steelmaking 33 (2006) 129–139, doi:10.1179/174328106X80127.
[8] A.P. Luz, C.G. Renda, A.A. Lucas, R. Bertholdo, C.G. Aneziris, V.C. Pandolfelli, Graphitization of phenolic resins for carbon-based refractories, Ceram. Int. 43 (2017) 8171–8182, doi:10.1016/j.ceramint.2017.03.143.
[9] W.E. Lee, 4.12 Refractories, (n.d.). 0-080437222.
[10] E. Brondoleze, M.E. Benocour, Behaviour during preheating of continuous casting refractories, 6 (2002).
[11] Y. Li, B.G. Thomas, Transient model of preheating a submerged entry nozzle, AISTech - Iron and Steel Tech. Conf. Proc. M (2014) 2907–2922.
[12] J.K.S. Svensson, A. Memarpour, V. Brabie, P.G. Jönsson, Studies of the decarburisation phenomena during preheating of submerged entry nozzles (SEN) in continuous casting processes, Ironmaking & Steelmaking 44 (2017) 108–116, doi:10.1080/03019233.2016.1156900.
[13] B. Chatterjee, K. Singh, Oxidation phenomena in carbon containing refractories and their protection, NML Tech. J. 34 (1992) 27–34.
[14] S. Vyazovkin, C.A. Wight, Isothermal and non-isothermal kinetics of thermally stimulated reactions of solids, Int. Rev. Phys. Chem. 17 (1998) 407–433, doi:10.1080/014423598230108.
[15] S. Vyazovkin, Model-free kinetics, J. Therm. Anal. Calorim. 83 (2006) 45–51, doi:10.1007/s10973-005-7044-6.
[16] F. Wang, Z. Huang, Y. Liu, Y. Li, Novel cardanol-containing boron-modified phenolic resin composites, High Perform. Polym. 29 (2017) 279–288, doi:10.1177/0954008316641196.
[17] J.M. Pérez, A. Fernández, Thermal stability and pyrolysis kinetics of lignin-phenol-formaldehyde resins, J. Appl. Polym. Sci. 123 (2012) 3036–3045, doi:10.1002/app.34817.
[18] A.H. Basta, M.Z. Sefain, N.A. El-Wakil, Kinetic studies on the pyrolytic degradation of phenolic resin paper sheets using dta technique. i. phenolic resins as beater additives, Polym. Plast. Technol .Eng. 33 (1994) 135–147, doi:10.1080/03602559408015291.
[19] M.v. Alonso, M. Oliet, J.C. Domínguez, E. Rojo, F. Rodríguez, Thermal degradation of lignin–phenol–formaldehyde and phenol–formaldehyde resol resins, J. Therm. Anal. Calorim. 105 (2011) 349–356, doi:10.1007/s10973-011-1405-0.
[20] F. Wang, L. Zhao, W. Fang, X. He, F. Liang, H. Chen, H. Chen, X. Du, Preparation of organic/inorganic composite phenolic resin and application in Al2O3-C refractories, Int. J. Appl. Ceram. Technol. 13 (2016) 133–139, doi:10.1111/ijac.12426.
[21] F. Rodriguez-Reinoso, P.L. Walker, Reaction of glassy carbon with oxygen, Carbon N. Y. 13 (1975) 7–10, doi:10.1016/0008-6223(75)90250-X.
[22] X. Bertran, G. Chollon, J. Dentzer, R. Gadiou, S. Fouquet, M.A. Dourges, F. Rebillat, Oxidation behavior at moderate temperature under dry and wet air of phenolic resin-derived carbon, Thermochim. Acta 649 (2017) 13–21, doi:10.1016/j.tca.2016.12.013.
[23] H.W. Chang, S.K. Rhee, Oxidation of carbon derived from phenolic resin, Carbon N. Y. 16 (1978) 17–20, doi:10.1016/0008-6223(78)90109-4.
[24] W. Lu, M.Y. Li, X.W. Li, X.X. Wu, L. bin Sun, Z.C. Li, Experimental study on the oxidation behavior and microstructural evolution of NG-CT-10 and NG-CT-20 nuclear graphite, Nucl. Sci. Tech. 30 (2019), doi:10.1007/s41365-019-0693-0.
[25] S. Vyazovkin, A.K. Burnham, J.M. Criado, L.A. Pérez-Maqueda, C. Popescu, N. Sbirrazzuoli, ICTAC Kinetics Committee recommendations for performing kinetic computations on thermal analysis data, Thermochim. Acta 520 (2011) 1–19, doi:10.1016/j.tca.2011.03.034.
[26] A. Khawam, D.R. Flanagan, Role of isoconversional methods in varying activation energies of solid-state kinetics: I. isothermal kinetic studies, Thermochim. Acta 429 (2005) 93–102, doi:10.1016/j.tca.2004.11.030.
[27] N. Sbirrazzuoli, Model-free isothermal and nonisothermal predictions using advanced isoconversional methods, Thermochim. Acta 697 (2021) 178855, doi:10.1016/j.tca.2020.178855.
[28] X. Li, B. Zhu, F. Zhao, In-situ synthesis of SiC and β-Si3Al3O3N5 whiskers in alumina carbon based materials, Mater. Sci. Forum 745–746 (2013) 663–666, doi:10.4028/www.scientific.net/MSF.745-746.663.
[29] G.E.A. Swann, S.V. Patwardhan, Application of Fourier Transform Infrared Spectroscopy (FTIR) for assessing biogenic silica sample purity in geochemical analyses and palaeoenvironmental research, Climate of the Past 7 (2011) 65–74, doi:10.5194/cp-7-65-2011.
[30] F. Kundie, C. Azhari, Z. Ahmad, Effect of nano- and micro-alumina fillers on some properties of poly(methyl methacrylate) denture base composites, J. Serb. Chem. Soc. 83 (2018) 75–91, doi:10.2298/JSC170118056K.
[31] M. Varga, T. Izak, V. Vretenar, H. Kozak, J. Holovsky, A. Artemenko, M. Hulman, V. Skakalova, D.S. Lee, A. Kromka, Diamond/carbon nanotube composites: raman, FTIR and XPS spectroscopic studies, Carbon N. Y. 111 (2017) 54–61, doi:10.1016/J.CARBON.2016.09.064.
[32] A.R. Abhijith, A.K. Srivastava, A. Srivastava, Synthesis and characterization of magnesium doped ZnO using chemical route, J. Phys. Conf. Ser. 1531 (2020), doi:10.1088/1742-6596/1531/1/012005.
[33] C. Fang, Y. Zhang, Z. Zhang, C. Shan, W. Shen, X. Jia, Preparation of "natural" diamonds by HPHT annealing of synthetic diamonds, CrystEngComm 20 (2018) 505–511, doi:10.1039/C7CE02013A.
[34] M. Kolahdoozan, R.J. Kalbasi, Z.S. Shahzeidi, F. Zamani, Knoevenagel condensation of aldehydes with ethyl cyanoacetate in water catalyzed by P4VP/Al 2 O 3 -SiO 2, J. Chem. 2013 (2013) 1–8, doi:10.1155/2013/496837.
[35] A. Boumaza, A. Djelloul, F. Guerrab, Specific signatures of α-alumina powders prepared by calcination of boehmite or gibbsite, Powder Technol. 201 (2010) 177–180, doi:10.1016/j.powtec.2010.03.036.
[36] H. Schulz, From the Kissinger equation to model-free kinetics: reaction kinetics of thermally initiated solid-state reactions, ChemTexts 4 (2018) 1–10, doi:10.1007/s40828-018-0062-3.
[37] G. Mishra, T. Bhaskar, Non isothermal model free kinetics for pyrolysis of rice straw, Bioresour. Technol. 169 (2014) 614–621, doi:10.1016/j.biortech.2014.07.045.
[38] A. Dhaundiyal, M.M. Hanon, Calculation of kinetic parameters of the thermal decomposition of residual waste of coniferous species: cedrus deodara, Acta Technologica Agriculturae 21 (2018) 75–80, doi:10.2478/ata-2018-0014.
[39] W.-.M. Guo, H.-.N. Xiao, G.-.J. Zhang, Kinetics and mechanisms of non-isothermal oxidation of graphite in air, Corros. Sci. 50 (2008) 2007–2011, doi:10.1016/j.corsci.2008.04.017.
[40] N.v. Muravyev, A.N. Pivkina, N. Koga, Critical appraisal of kinetic calculation methods applied to overlapping multistep reactions, Molecules (2019) 24, doi:10.3390/molecules24122298.
[41] N. Sbirrazzuoli, L. Vincent, J. Bouillard, L. Elegant, Isothermal and non-isothermal kinetics when mechanistic information available, J. Therm. Anal. Calorim. 56 (1999) 783–792, doi:10.1023/A:1010110307418.
[42] Z. Yao, S. Yu, W. Su, W. Wu, J. Tang, W. Qi, Kinetic studies on the pyrolysis of plastic waste using a combination of model-fitting and model-free methods, Waste Manage. Res. 38 (2020) 77–85, doi:10.1177/0734242X19897814.
[43] A.O. Balogun, A.A. Adeleke, P.P. Ikubanni, S.O. Adegoke, A.M. Alayat, A.G. McDonald, Kinetics modeling, thermodynamics and thermal performance assessments of pyrolytic decomposition of Moringa oleifera husk and Delonix regia pod, Sci. Rep. 11 (2021) 13862, doi:10.1038/s41598-021-93407-1.
[44] X. Zhou, C.I. Contescu, X. Zhao, Z. Lu, J. Zhang, Y. Katoh, Y. Wang, B. Liu, Y. Tang, C. Tang, Oxidation behavior of matrix graphite and its effect on compressive strength, Sci. Tech. Nucl. Instal. 2017 (2017) 1–6, doi:10.1155/2017/4275375.
[45] J. Xu, J. Yang, X. Liu, H. Wang, J. Zhang, S. Fu, Preparation and characterization of fast-curing powder epoxy adhesive at middle temperature, R. Soc. Open Sci. 5 (2018), doi:10.1098/rsos.180566.

[46] B. Luchini, J. Grabenhorst, J. Fruhstorfer, V.C. Pandolfelli, C.G. Aneziris, On the nonlinear behavior of Young's modulus of carbon-bonded alumina at high temperatures, J. Am. Ceram. Soc. 101 (2018) 4171–4183, doi:10.1111/jace.15575.
[47] J. Werner, C.G. Aneziris, S. Dudczig, Young's modulus of elasticity of carbon-bonded alumina materials up to 1450 °C, J. Am. Ceram. Soc. 96 (2013) 2958–2965, doi:10.1111/jace.12526.
[48] S. Vyazovkin, Determining preexponential factor in model-free kinetic methods: how and why? Molecules 26 (2021) 3077, doi:10.3390/molecules26113077.
[49] D. Drozin, S. Sozykin, N. Ivanova, T. Olenchikova, T. Krupnova, N. Krupina, V. Avdin, Kinetic calculation: software tool for determining the kinetic parameters of the thermal decomposition process using the Vyazovkin Method, SoftwareX 11 (2020) 100359, doi:10.1016/j.softx.2019.100359.
[50] P. Mallet-Ladeira, P. Puech, C. Toulouse, M. Cazayous, N. Ratel-Ramond, P. Weisbecker, G.L. Vignoles, M. Monthioux, A Raman study to obtain crystallite size of carbon materials: a better alternative to the Tuinstra-Koenig law, Carbon N. Y. 80 (2014) 629–639, doi:10.1016/j.carbon.2014.09.006.
[51] M.A. Pimenta, G. Dresselhaus, M.S. Dresselhaus, L.G. Cançado, A. Jorio, R. Saito, Studying disorder in graphite-based systems by Raman spectroscopy, Phys. Chem. Chem. Phys. 9 (2007) 1276–1290, doi:10.1039/B613962K.
[52] O.A. Maslova, M.R. Ammar, G. Guimbretière, J.N. Rouzaud, P. Simon, Determination of crystallite size in polished graphitized carbon by Raman spectroscopy, Phys. Rev. B Condens. Matt. Mater. Phys. (2012) 86, doi:10.1103/PhysRevB.86.134205.
[53] R. Krishna, A.N. Jones, R. Edge, B.J. Marsden, Residual stress measurements in polycrystalline graphite with micro-Raman spectroscopy, Radiation Physics and Chemistry. 111 (2015) 14–23. 10.1016/j.radphyschem.2015.02.007.
[54] B. Estandia, L. Rodriguez, J.A. Alvarez, D. Ferreño, D. Hernández, J. Gonzalez, Raman spectroscopy of flake graphite as a tool to detect stress-strain states in cast iron, 71st World Foundry Congress: Advanced Sustainable Foundry, WFC 2014, 2014.
[55] M. Sharma, S. Rani, D.K. Pathak, R. Bhatia, R. Kumar, I. Sameera, Temperature dependent Raman modes of reduced graphene oxide: effect of anharmonicity, crystallite size and defects, Carbon N. Y. 184 (2021) 437–444, doi:10.1016/J.CARBON.2021.08.014.
[56] K. Alamelu, V. Raja, L. Shiamala, B.M. Jaffar Ali, Biphasic TiO 2 nanoparticles decorated graphene nanosheets for visible light driven photocatalytic degradation of organic dyes, Appl. Surf. Sci. 430 (2018) 145–154, doi:10.1016/j.apsusc.2017.05.054.
[57] R. Rahimi, S. Zargari, Z. Sadat Shojaei, Photoelectrochemical investigation of TiO2-graphene nanocomposites, in: Proceedings of The 18th International Electronic Conference on Synthetic Organic Chemistry, MDPI, Basel, Switzerland, 2014, p. a044, doi:10.3390/ecsoc-18-a044.
[58] W.W. So, S. bin Park, K.J. Kim, C.H. Shin, S.J. Moon, The crystalline phase stability of titania particles prepared at room temperature by the sol-gel method, J. Mater. Sci. 36 (2001) 4299–4305, doi:10.1023/A:1017955408308.
[59] M. Aguilar-Pujol, R. Ramírez-Jiménez, E. Xifre-Perez, S. Cortijo-Campos, J. Bartolomé, L.F. Marsal, A. de Andrés, Supported ultra-thin alumina membranes with graphene as efficient interference enhanced raman scattering platforms for sensing, Nanomaterials 10 (2020) 830, doi:10.3390/nano1005083.